

Article

The Effect of Iron- and Calcium-Rich Waste Rock's Acid Baking Conditions on the Rare-Earth Extraction

Vitor L. Gontijo ¹, Leandro Augusto Viana Teixeira ² and Virgínia Sampaio Teixeira Ciminelli ^{1,3,*}¹ Acqua Institute, Belo Horizonte 31270-901, MG, Brazil² Vale S.A, Innovation Strategy and Ecosystem, Nova Lima 34006-270, MG, Brazil³ School of Engineering, Universidade Federal de Minas Gerais, Belo Horizonte 31270-901, MG, Brazil

* Correspondence: ciminelli@demet.ufmg.br

Highlights:

- Effect of low-temperature sulfation, H₂SO₄ to ore ratio and time on REE extraction.
- Differences in REE host minerals and their impact on these elements extraction.
- Increasing sulfuric acid availability reduces iron dissolution from Fe-rich sample.
- Inhibitory effect on the crystallization of Ca-sulfate by REE uptake during leaching.

Abstract: The work investigates the effect of sulfuric acid baking on rare earth element (REE) extraction from two waste rock samples from a phosphate mine. The role of different mineralogical assemblages and the degree of alteration (i.e., weathering), and the behavior of the main impurities—iron, phosphorus, and calcium—on REE extraction are emphasized. For both samples, the sulfuric acid baking at 25 °C, during 15 min, H₂SO₄:sample (*w/w*) mass ratio of 0.45:1 is the best condition for achieving the selective leaching of REE. For the iron rich-sample, the increase in temperature reduces REE extraction and increases iron dissolution. The corresponding sulfuric acid consumed by goethite (α-FeOOH) from 25 °C to 160 °C acid baking is ten times higher than that required for the monazite (REEPO₄) reaction. Conversely, higher REE and lower iron extraction are observed by increasing (sulfuric acid/sample) mass ratio (0.95:1). Due to the high sulfuric concentration during dissolution, a local saturation zone close to the dissolution front caused the precipitation of iron oxyhydroxides. The calcium-rich sample shows lower REE extraction by leaching (63% maximum) mainly due to the entrapment of REE-bearing minerals by a gypsum layer, and lanthanide's uptake by calcium sulfate compounds formed during leaching. The results were discussed with the help of a detailed characterization of the residues.

Keywords: sulfuric acid-baking; rare earth element; calcium sulfate; by-product; monazite; apatite



Citation: Gontijo, V.L.; Teixeira, L.A.V.; Ciminelli, V.S.T. The Effect of Iron- and Calcium-Rich Waste Rock's Acid Baking Conditions on the Rare-Earth Extraction. *Minerals* **2023**, *13*, 217. <https://doi.org/10.3390/min13020217>

Academic Editors: Kenneth N. Han and Kwadwo Osseo-Asare

Received: 5 January 2023

Revised: 30 January 2023

Accepted: 31 January 2023

Published: 2 February 2023



Copyright: © 2023 by the authors. Licensee MDPI, Basel, Switzerland. This article is an open access article distributed under the terms and conditions of the Creative Commons Attribution (CC BY) license (<https://creativecommons.org/licenses/by/4.0/>).

1. Introduction

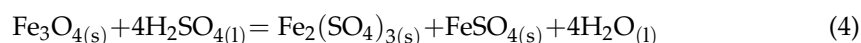
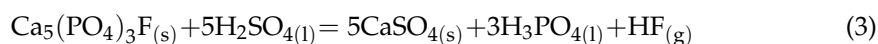
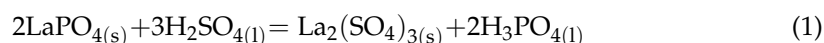
The distinguishing role of rare earth elements (REE) in the clean energy industry makes them a key point for the recent global movement towards electrification. The major contribution of these elements is in the production of catalysts, permanent magnets, phosphors, metal alloys for rechargeable batteries, and ceramic materials [1–3]. Therefore, several studies addressed the recovery of these elements from secondary sources or as a by-product [4–7], from tailings [8–10], and recycling end-of-life products [11–13].

The main reserves of REE in Brazil are located in alkaline carbonatite, granitic formations, and marine placers. The placer-type deposits are found across all the Brazilian coastline, and the most important reserves are in the Southeast region (i.e., *Espírito Santo* and north of *Rio de Janeiro*). Carbonatites and alkaline rocks are found mainly in the south-east, central-west and north regions (i.e., *Minas Gerais*, *Goiás*, *São Paulo* and *Amazonas*). The REE-carrying minerals in the different provinces of Brazil are primarily monazite and secondly bastnasite. The content of rare earth oxides (REO) varies from 1.0% to 8.0%,

depending on the deposit [14–16]. Due to the similarity of the REE and calcium's ionic radii, substitutions can occur in the crystalline structure of apatite ($\text{Ca}_5(\text{PO}_4)_3(\text{F},\text{Cl},\text{OH})$). Thus, apatite from igneous and metamorphic rocks can also be an important source of lanthanides [17].

One drawback of using calcium-rich samples to recover REE is related to the high sulfate concentration in the leach solution. The purification of the solution to remove calcium is carried out by the precipitation of gypsum ($\text{CaSO}_4 \cdot 2\text{H}_2\text{O}$), which could result in lanthanide uptake by gypsum during precipitation [18]. The mechanisms of REE uptake by gypsum are controversial as some say it involves co-precipitation others adsorption. The presence of elevated iron content is another issue in REE extraction due to the reaction of minerals, such as goethite ($\alpha\text{-FeOOH}$) (2) and magnetite (Fe_3O_4) (4) with sulfuric acid [19] resulting in an increase in acid consumption. High-temperature treatment prior to leaching is an option for reducing iron dissolution [20–23]. Although sulfuric acid baking is a well-established process in the literature and in the industry, few studies investigated the process at low-temperature (i.e., temperatures $< 300^\circ\text{C}$, [24]).

During baking, the overall reactions for a generic lanthanum phosphate (i.e., monazite), goethite, fluorapatite, and magnetite with concentrated sulfuric acid are as follows:



After baking, the solids are contacted with water; impurities, such as iron and calcium, are leached to some extent, together with the REE. Minimizing impurities dissolution during leaching means less burden and costs associated with the purification stages that follow leaching.

There is a lack of fundamental studies on the pre-treatment procedures (e.g., sulfation) applied to different REE sources as well as the effect of major impurities on the subsequent REE leaching. This work evaluates the sulfation and leaching of two REE samples with different mineralogical assemblages and degree of alteration (i.e., weathered material), as a function of sulfation temperature, H_2SO_4 :sample (w/w) mass ratio, and time. The extraction of REE-carrying minerals and impurities are investigated with a focus on the behavior of iron- and calcium-rich minerals. A better understanding of the effect of these compounds on the sulfation and leaching of REE, supported by a detailed characterization of the residues is expected to contribute to the processing of other secondary and complex REE sources.

2. Materials and Experimental Procedure

2.1. Materials

The selected samples originated from an igneous phosphate operating mine in *Triângulo Mineiro*, Minas Gerais/Brazil, which are: two natural fines ($<74\ \mu\text{m}$) of monazite (Bebedourite-BEDE) and fluorapatite (Silexite-SILX). These materials are not a target ore for fertilizer and are thus seen as potential REE sources. Sulfuric acid (*Química Moderna*, 95%–98% w/v), nitric acid (*Química Moderna*, 65% w/v) and Milli-Q water (electrical conductance of 18 $\text{M}\Omega\ \text{cm}$) were used in all tests.

2.2. Experimental Procedures

The experimental procedure used in the rare-earths extraction comprised six stages: (i) heating, (ii) sulfation, (iii) leaching, (iv) centrifuge separation, (v) washing of the leaching residue, and (vi) vacuum filtration. Firstly, 30.0 g of the natural fines samples were weighted in a 100 mL porcelain crucible and heated in a muffle (Lavoisier) at predefined temperatures (80, 160 and 240°C) for 15 h. The time was defined to ensure that the samples

were at the test temperature before the addition of concentrated sulfuric acid (95%–98% w/v). Four sulfation times ($t = 0, 15, 30$ and 60 min), and three mass ratios (w/w) of H_2SO_4 :sample (0.45:1, 0.72:1, 0.95:1) were assessed. The set (i.e., heated sample and sulfuric acid) was manually homogenized and returned to the muffle at the same temperature as the heating step. The sulfation product proceeded to the leaching stage without prior cooling or grinding.

The leaching step was performed in a 0.9 mol L^{-1} H_2SO_4 solution with an initial mass ratio (w/w) sample:solution of 1:9, which is equivalent to approximately 10% solids. The time of 2 h used for the leaching step followed the procedure reported by [19,21]. After the addition of the sulfation product, the temperature of the leaching solution remained between 30 ± 3 °C during the entire reaction time. After leaching, the pulp was then transferred to 50 mL Falcon tubes and placed in a centrifuge to separate the liquor from the residue. The conditions used for this step consist of 15 min under a rotation of 4000 rpm. The liquor was poured into an Erlenmeyer and weighed, and the leach residue went onto the washing stage.

The washing stage was performed to remove all remnants of the solution that were retained in the residue. This step was carried out in two stages, each one consisting of the addition of 270 g of Milli-Q water followed by magnetic stirring for 20 min. At the end of each washing stage, the pulp was transferred to 50 mL Falcon tubes and then to the centrifuge under the same conditions as previously described. The final washed residue was then filtered under vacuum using 270 g of Milli-Q water, using a quantitative JP42 blue band filter paper with a pore size of 8 μm and the wet cake was placed in a laboratory oven at 60 °C overnight. The repeatability of the results was firstly evaluated (at 25 °C, 30 min, H_2SO_4 :sample ratio of 0.45:1(w/w)) by triplicates (standard deviation < 5%); all the remained tests were carried out in duplicates. The extraction/dissolution percentages refer to the amount of a given element leached, after sulfation, relatively to its content in the feed sample.

2.3. Analytical Methods

Particle size distribution was undertaken by a laser diffraction granulometer (Cilas, model 1064). Specific surface area (SSA) was determined by the multipoint Brunauer-Emmett-Teller (BET) method through nitrogen adsorption (Quantachrome NOVA 1200e) after degassing the samples at 90 °C. The samples and leach residues were analyzed by X-ray diffraction (XRD) (Philips, Panalytical PW1710) using Cu anode ($K_{\alpha 1} = 1.54059$ Å) in a 2θ angle range from 3.0200° to 89.9400° with a scan step size of $0.040^\circ \text{ s}^{-1}$, tube voltage of 35 kV and current of 50 mA. Mineral identification was made using the Inorganic Crystal Structure Database (ICSD), and Crystallography Open Database (COD). The (h k l) Miller indexes were identified using VESTA software (Visualization for Electronic and Structural Analysis). The mineralogical characterization, modal composition, and mineralogical association were performed by XRD, Scanning Electron Microscopy (SEM), and Quantitative Evaluation of Minerals by Scanning Electron Microscopy (QEMSCAN). Polished sections were prepared for QEMSCAN and SEM analysis. Raman spectroscopy (Jobin Yvon Horiba, LabRam-HR800) was used to characterize a fine precipitate formed during liquor storage. The spectra varied between 100 and 1200 cm^{-1} with a step size of 1 cm^{-1} ; a minimum of 30 scans of 30 s each were recorded.

Chemical analyses of the samples and the leaching residues were carried out after fusion with lithium metaborate (LiBO_2) and acid digestion ($\text{C}_4\text{H}_6\text{O}_6$ and HNO_3). The solutions were analyzed by Inductively Coupled Plasma Optical Emission Spectroscopy (ICP-OES) (Perkin Elmer, model Optima 7300DV) and Inductively Coupled Plasma Mass Spectroscopy (ICP-MS) for major and minor elements, respectively, as well as for the diluted and washing solutions. Dilution factors were calculated using the values of the upper detection limit of the equipment and making sure that the final concentration was below the solubility limit for the major impurities' compounds (e.g., ferric phosphate and calcium sulfate). The liquor was diluted 65x for BEDE and 35x for SILX samples with a

final nitric acid (HNO_3) concentration solution of 10% (w/v), whereas for the washing solution, concentrate HNO_3 (65%) was added directly into the recipient, which resulted in a final 5% (w/v) acid concentration. Dilution was only performed for analytical purposes. The final residue was transferred into a porcelain mortar and ground to reduce the nugget effect in the homogenization stage. In the end, the residue was homogenized and directed to chemical analysis. Two certified reference materials and blank control were used to evaluate the accuracy of the chemical analysis.

3. Results

3.1. Characterization of the As-Received Samples

The two samples from an igneous phosphate deposit in west Minas Gerais/Brazil have considerable REE content. The main difference refers to the samples' weathered condition, hence their mineral assemblage. Bebedourite (BEDE) is a sample rich in iron and REE, and the silexite (SILX) a REE by-product from a phosphate ore (apatite) zone enriched in silica.

According to Soubiès [25], the weathering of fresh rock follows a sequence of transformations, which are: (i) perovskite into anatase, (ii) dissolution of apatite, replaced by secondary phosphates from the crandallite group, (iii) magnetite into iron oxyhydroxides, (iv) biotite kaolinization, and (v) total replacement/dissolution of pyroxene and olivine. BEDE is found in the isalterite/alloterite levels between the fresh rock and the soil horizons. This region is characterized by the predominance of iron oxyhydroxides, phosphates, minerals from supergenic alteration (e.g., anatase), and minor phyllosilicates (e.g., muscovite, biotite and phlogopite) [26]. Figure 1 shows the XRD diffraction patterns for the studied samples. The samples' mineral composition was determined by Quantitative Evaluation of Minerals by Scanning Electron Microscopy (QEMSCAN) and shown in Figure 2. The consistency of mineral composition was checked with the chemical composition (Table 1) and XRD (Figure 1).

For BEDE, monazite-rhabdophane ($(\text{REE})\text{PO}_4\text{-(REE)PO}_4\cdot 0.5\text{H}_2\text{O}$) are the main REE-bearing minerals. Other major constituents are quartz (SiO_2), goethite ($\alpha\text{-FeOOH}$), ilmenite (FeTiO_3) and anatase (TiO_2). In a previous investigation, [21] also reported the presence of approximately 5% (w/w) of crandallite ($\text{CaAl}_3(\text{OH})_6(\text{PO}_4)_2\text{H}$), a rare earth carrier, but the mineral was not identified by XRD. Due to the heterogeneity of the sample, the identification of crandallite may be challenging.

The other phosphate mineralization zone, SILX, occurs in the region above the fresh rock, which is formed by altered pyroxenite and silexite [27]. Apatite ($\text{Ca}_5(\text{PO}_4)_3(\text{OH}, \text{F}, \text{Cl})$) is the predominant phosphate mineral whereas the accessory minerals are quartz, goethite and titanomagnetite ($\text{Fe}^{2+}(\text{Fe}^{3+}, \text{Ti})_2\text{O}_4$). Relatively to the BEDE, the mineralogical phases identified in SILX are consistent with a lower degree of weathering.

Table 1 shows the chemical composition of the samples. The BEDE has the highest iron (45.6% Fe_2O_3) and rare earth oxides (REO) (7.4%) content of the studied samples. SILX shows an expressive content of CaO (24.9%) and P_2O_5 (19.5%), that together with fluorine (1.4% F) indicates the apatite variation of fluorapatite ($\text{Ca}_5(\text{PO}_4)_3\text{F}$, ~40%). The REE content is 2.1% REO. Regarding the content of radionuclide elements (Th and U), there is a wide range for thorium (70–480 mg kg^{-1}), and similar content for uranium (99–120 mg kg^{-1}). The mineralogical characterization and the chemical composition of the samples are in accordance with the mineral distribution (QEMSCAN) shown in Figure 2.

The QEMSCAN (Figure 2) analysis indicates iron oxides, mainly goethite according to Figure 1, as the major constituents of BEDE. Iron is also found in ilmenite. The REE carrier minerals, monazite and crandallite were identified. The latter corresponds to 7.5 wt. % in this sample [21]. For the SILX, in addition to the main phases identified (i.e., apatite and quartz), minor monazite was also observed.

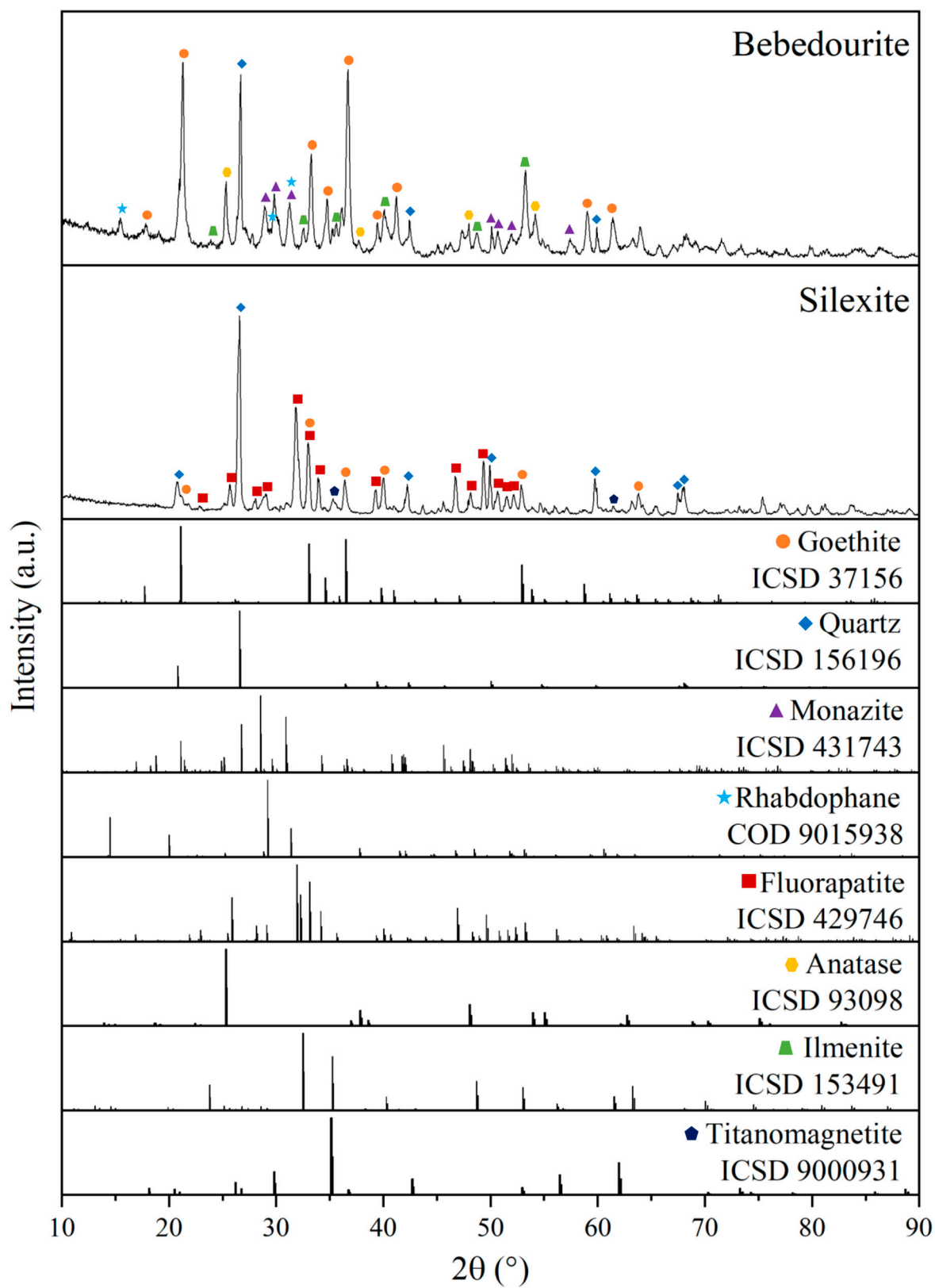


Figure 1. X-ray diffractograms of the as-received samples. (Cu (Kα) radiation, tube voltage of 35 kV and current of 50 mA).

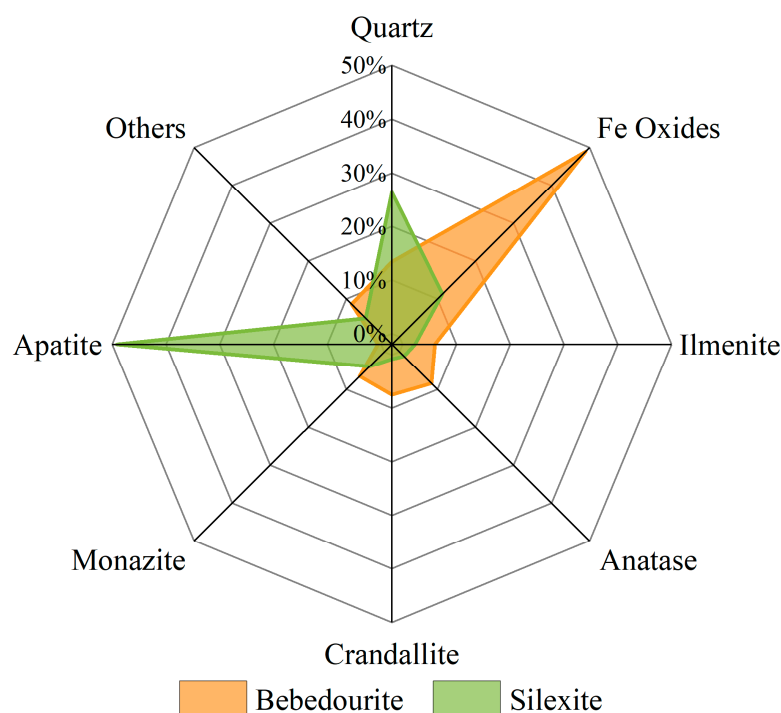


Figure 2. Mineral distribution (QEMSCAN) diagram of the as-received samples.

Table 1. Chemical composition (%Me_xO_y) of the as-received samples.

Chemical Composition (%)	Bebedourite	Silixite
Al ₂ O ₃	4.0	0.8
BaO	2.4	0.4
CaO	0.9	24.9
Fe ₂ O ₃	45.6	17.2
MgO	0.3	0.6
MnO	1.3	0.6
P ₂ O ₅	7.2	19.5
SiO ₂	10.9	27.0
TiO ₂	11.0	2.7
F	0.2	1.4
Others ¹	1.0	0.3
U (mg kg ⁻¹)	99.0	119.5
Th (mg kg ⁻¹)	479.7	70.7
REO ²	7.4	2.1
LREE ³ /REE _{Total}	98.9	98.8
LOI	7.8	2.5

¹ Cr₂O₃, K₂O, Na₂O, ZrO. ² REO—rare earth oxides. ³ LREE—light rare earth elements.

The samples were further evaluated via SEM images to characterize the REE carrier minerals. The supplementary material (Figures S1–S4) shows the chemical mappings of the particles. For the BEDE, monazite is dispersed in the sample in a concentric globular texture. The association of monazite with secondary phases (i.e., crandallite, goethite and ilmenite) is expected as the alteration towards the topsoil increases. Crandallite, a calcium aluminum basic secondary phosphate mineral, is indicated by SEM chemical mapping (Figure S2). The presence of cerium within this mineral phase is shown. The REE carrier minerals for the BEDE are associated with iron phases; the images suggest interstitial and oxyhydroxide surface layers on crandallite (Figures S1 and S2). Conversely, for the SILX, the REE carriers are found as free particles (Figure S3). The SILX polished sections showed REE associated with monazite (Figure S3) with a minor occurrence in apatite, likely fluorapatite

according to the chemical analysis (Figure S4). Associations with iron compounds have not been detected.

Table 2 shows the BEDE relatively fine particle sizes and high specific surface area (SSA). BEDE comprises a fine particulate material, approximately 65% of the sample is below 10 μm , with an average diameter of 8.8 μm , and a top size of 35 μm . The SILX is also a fine material, 43% below 10 μm , with an average diameter of 18.2 μm , and a top size of 70 μm . The SSA analysis was performed with the samples at room temperature ($\text{SSA}_{25\text{ }^\circ\text{C}}$) and after heating at 240 $^\circ\text{C}$ ($\text{SSA}_{240\text{ }^\circ\text{C}}$) for 15 h. Both samples contain hydrated minerals that can be transformed into new phases at higher temperatures. This transformation occurs through the rearrangement of the crystalline structures after the loss of structural water, which alters the molar volume and leads to differences in the SSA. After heating, goethite is transformed into hematite, increasing its SSA [19]. For both samples, there is an increase of approximately 1.5x after heating. BEDE depicted the largest surface areas ($\sim 22\text{--}32\text{ m}^2\text{ g}^{-1}$, 1.5x). Goethite and monazite, both occurring as fine particles and being the former also amenable to phase transformation, contributed to this finding. Conversely, the presence of coarser particles is reflected on the lower SILX SSA ($\sim 6\text{--}8\text{ m}^2\text{ g}^{-1}$, 1.4x).

Table 2. Particle size distribution and specific surface area (SSA) data for the samples.

Sample	BEDE	SILX
d_{10} (μm)	0.6	1.0
d_{50} (μm)	5.0	13.5
d_{90} (μm)	22.7	43.7
Mean diameter (μm)	8.8	18.2
$\text{SSA}_{25\text{ }^\circ\text{C}}$ ($\text{m}^2\text{ g}^{-1}$)	21.9	5.7
$\text{SSA}_{240\text{ }^\circ\text{C}}$ ($\text{m}^2\text{ g}^{-1}$)	32.3	7.9

The morphology of the BEDE's mineral phases provided by SEM images show coarser particles for iron, titanium, and silica-rich compounds, whereas goethite was also found as a fine particulate. For the REE-carrier minerals, monazite particles were found in sizes below 10 μm . The grains, dispersed throughout the sample, depicted an altered and porous texture and no well-defined boundaries. Crandallite, on the other hand, were found as coarser particles up to 30 μm , with porous texture and more defined boundaries. For the SILX, the alteration in fluorapatite and monazite' texture is less evident. These phases look compact with some fractures inward of the core. The particle size distribution varies (30 μm to <10 μm), which could be due to the high silica content, a mineral less amenable to milling. Therefore, a heterogeneous range of particle sizes was produced.

3.2. Implications in Rare Earth Element Extraction Associated with Impurities

Different proportions of major constituents that are amenable to react with sulfuric acid are evident in each sample (Table 1). The REE carriers are also different (monazite and crandallite vs. fluorapatite), which can directly impact the reactivity with H_2SO_4 , hence affecting the recovery of the target elements. The effect of the different mineral assemblages, temperature, H_2SO_4 :sample mass ratio (w/w) and time over low-temperature sulfation on REE extraction was assessed. At the end, the best condition for the selective REE extraction relative to iron, calcium and phosphorus will be discussed.

3.2.1. Effect of Temperature

Figure 3 depicts the element extraction/dissolution for each sample at different temperatures, using the H_2SO_4 :sample mass ratio of 0.45:1 and 30 min sulfation. For BEDE (Figure 3a), the lowest iron dissolution (14%—5.5 g L^{-1}) and the highest REE extraction (87%—Ce + La = 4.1 g L^{-1} , Nd + Pr = 1.5 g L^{-1}) are observed at the lowest (25 $^\circ\text{C}$) sulfation temperature. There is an increase in iron dissolution with temperature until a plateau at 33% iron extraction (10.3 g L^{-1} Fe) is reached at 80 $^\circ\text{C}$. Conversely, REE extraction reaches a minimum at 160 $^\circ\text{C}$ (63% Ce + La = 3.1 g L^{-1} , Nd + Pr = 1.2 g L^{-1}). Calcium

extraction increases whereas phosphorus is unaffected by the sulfation temperature and remains nearly constant. At 240 °C the maximum element dissolution reached 63% for Ca (0.5 g L⁻¹) and 48% for P (1.7 g L⁻¹).

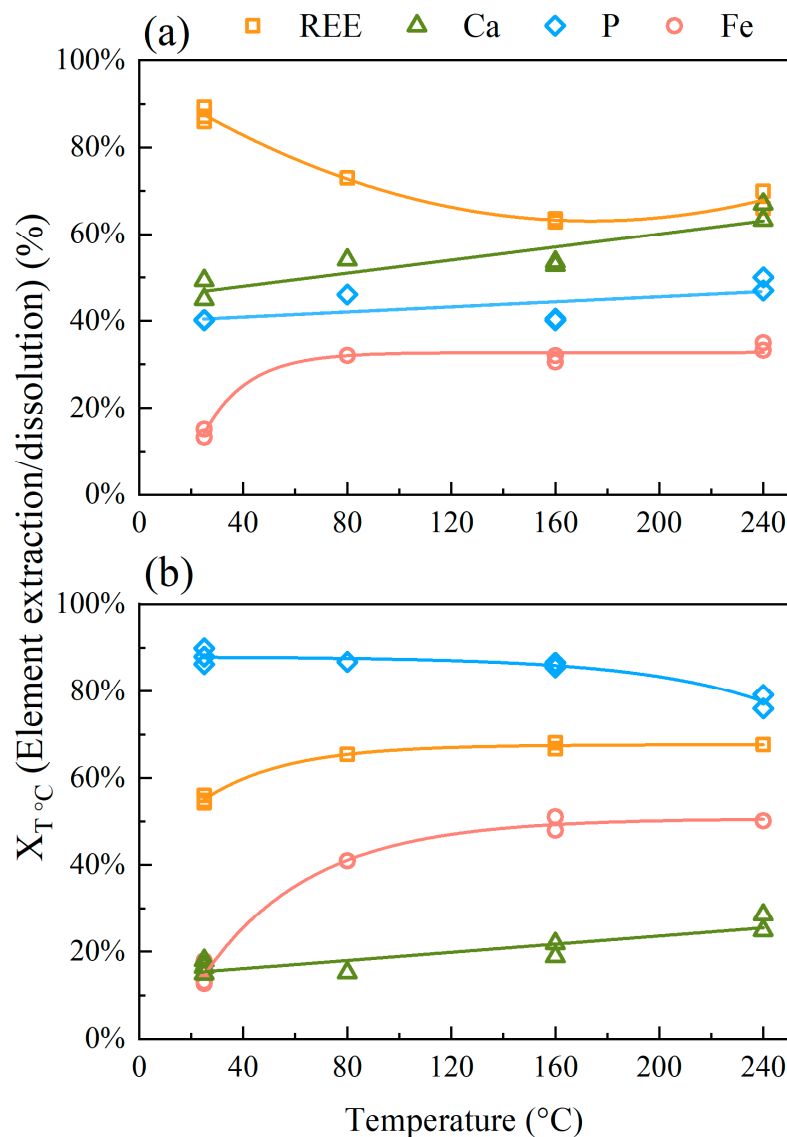


Figure 3. The effect of sulfation temperature on the element extraction for (a) BEDE and (b) SILX (30 min sulfation, with H₂SO₄:sample (*w/w*) of 0.45:1; leaching at 30 ± 3 °C in 0.9 mol L⁻¹ H₂SO₄ for 2 h with initial sample:solution ratio (*w/w*) of 1:9). X_{T °C} (%) refers to the element extraction/dissolution at the predefined temperature.

For sulfation at room temperature, the SILX sample (Figure 3b) depicted approximately 17% calcium (4.2 g L⁻¹) and iron (1.4 g L⁻¹), 86% phosphorus (9.0 g L⁻¹) dissolution, and 55% REE extraction (Ce + La = 1.3 g L⁻¹, Nd + Pr = 0.4 g L⁻¹). Upon temperature rise, there is a slight increase followed by the stabilization in the REE (67%, between 1.5 to 2.0 g L⁻¹) and Fe (45%, 6.8 g L⁻¹) dissolution, with a less significant increase in REE (X_{240 °C}/X_{25 °C} = 1.2) than Fe (X_{240 °C}/X_{25 °C} = 2.8). In relation to P, the results show an 8% reduction in the dissolution at room temperature (i.e., 90% and 9.5 g L⁻¹ P) and for calcium, an increase in dissolution to approximately 25%, both at 240 °C. The main feature in the SILX leaching is the high P extraction relative to REE, Fe and Ca in all temperatures.

3.2.2. Effect of H₂SO₄:Sample Mass Ratio

For both samples, a sub-stoichiometric sulfuric acid:solid ratio of 0.45:1 (*w/w*) was used in the temperature experiments discussed above. In that matter, different ratios—calculated according to the content of acid-consuming compounds—were evaluated to verify the extraction/dissolution behavior of each element. The H₂SO₄:solid (*w/w*) stoichiometric ratio for the BEDE and SILX samples are 0.95:1 and 0.72:1, respectively. Figure 4 presents the results for the H₂SO₄:sample ratios at 25 °C and 30 min sulfation for both samples.

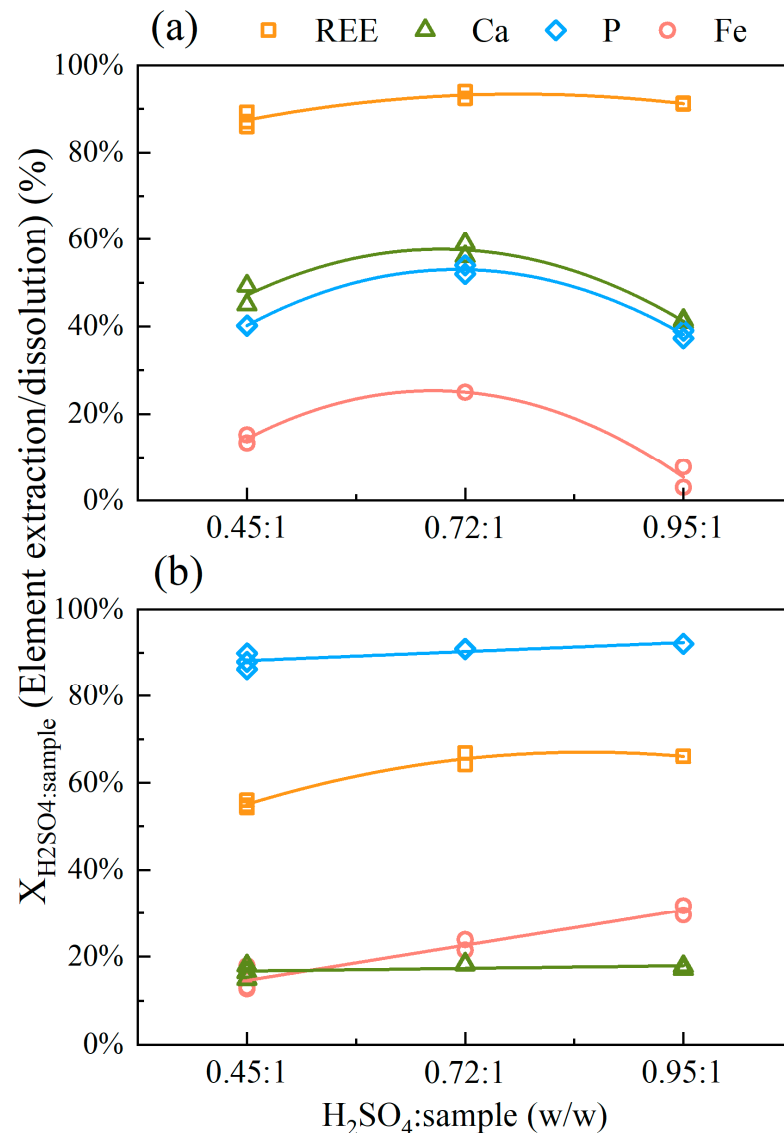


Figure 4. Effect of sulfuric acid to sample ratio in the sulfation. Element extraction for (a) BEDE and (b) SILX. (30 min sulfation at 25 °C, leaching at 30 ± 3 °C in 0.9 mol L⁻¹ for 2 h with initial sample:solution (*w/w*) of 1:9). $X_{\text{H}_2\text{SO}_4:\text{sample}}$ (%) refers to the element extraction/dissolution at the predefined ratios.

A point of maximum dissolution was observed for the BEDE at a sub-stoichiometric 0.72:1 ratio. REE extraction reached 93% (Ce + La = 4.5 g L⁻¹, Nd + Pr = 1.7 g L⁻¹) with 57% Ca (0.4 g L⁻¹), 53% P (1.8 g L⁻¹) and 25% Fe (8.9 g L⁻¹) dissolution. For the 0.95:1 mass ratio, BEDE depicted the lowest iron (6%–2.7 g L⁻¹) and phosphorus/calcium (40%–1.3 and 0.3 g L⁻¹, respectively) dissolution and 91% REE extraction (Figure 4a). Despite the low iron and phosphor dissolution, the sulfation product was difficult to handle due to agglomeration. This implies operational problems (e.g., scaling in the rotary kiln) in addition to relatively large acid consumption. According to Verbaan et al. [28], a lower

metal recovery is sometimes necessary so the sulfated material can have a better handling characteristic. No significant variations in REE extraction were observed by increasing the H_2SO_4 :sample mass ratio.

For the SILX, the increase in acid addition did not significantly change the dissolution of Ca and P. However, the latter depicts the highest dissolution among the main elements (Figure 4b). Each mole of fluorapatite reacting with sulfuric acid produces three moles of phosphoric acid (Reaction 3), which explains the high phosphorus concentration in the system. In addition, the formation of calcium sulfate is also expected to occur in systems containing sulfate. Hence, calcium dissolution does not vary and remains at approximately 18% (4.0 g L^{-1}). The REE extraction depicted a subtle increase associated with increased acid:solid ratio, whereas iron a linear and positive increase. At 0.95:1 ratio, the former reached a maximum extraction of 66% ($\text{Ce} + \text{La} = 1.1 \text{ g L}^{-1}$, $\text{Nd} + \text{Pr} = 0.35 \text{ g L}^{-1}$), and the latter of 31% (4.6 g L^{-1}).

3.2.3. Effect of Time

Figure 5 presents the results for different sulfation times with 0.45:1 H_2SO_4 :solid (w/w) ratio at 25°C for both samples. Demol et al. [29] reviewed the sulfuric acid bake processing and, overall, the residence times were reported in a range of 0.5–5 h. The reasons for this broad time range were not discussed, but one may assume that the degree of weathering, mineral carrier and REE content could play a fundamental role in the sulfation processing time.

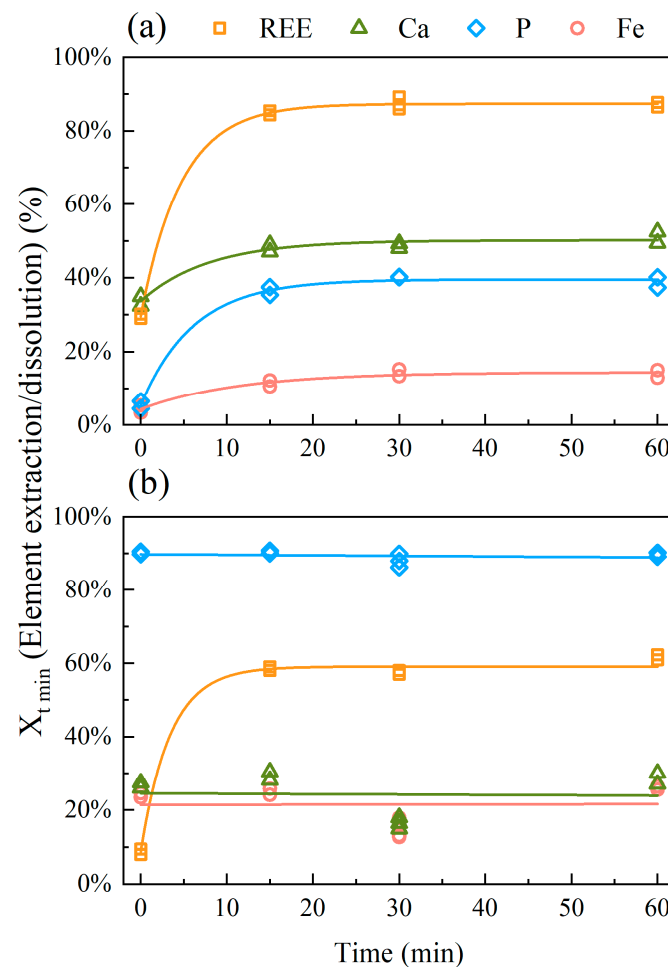


Figure 5. Effect of sulfation time. Element extraction for (a) BEDE and (b) SILX. (H_2SO_4 :sample (w/w) of 0.45:1 at 25°C , leaching at $30 \pm 3^\circ\text{C}$ in 0.9 mol L^{-1} for 2 h with initial sample:solution (w/w) of 1:9). $X_{t \text{ min } ^\circ\text{C}}$ (%) refers to the element extraction/dissolution at the predefined times.

At sulfation time $t = 0$ min, the extraction refers only to the element dissolution in the $0.9 \text{ mol L}^{-1} \text{ H}_2\text{SO}_4$ leaching solution without acid baking. It is interesting to note that 30% of REE (2.0 g L^{-1}) is extracted by the leaching solution alone (no baking), but phosphorus remained at 4.5% dissolution (0.15 g L^{-1}) for BEDE. The molar ratio REE/P in solution is equal to 3.0, which is higher than that in monazite (La:P = 1:1). Based on this finding and the low iron dissolution (3.4%, 1.1 g L^{-1}) it is assumed that $\text{FePO}_4 \cdot 2\text{H}_2\text{O}_{(s)}$ precipitates, as will be further discussed. Increasing the sulfation time leads to a rapid increase in the dissolution of all the sulfate salts. The sulfation proceeds rapidly and reaches a plateau with the highest conversions (approximately 85% REE, 50% Ca, 35% P and 12% Fe) achieved within 15–20 min for all elements. The SILX depicted the lowest REE extraction (9.4%, 0.21 g L^{-1}) in contrast with the highest dissolution of impurities that remained constant with increasing time. Phosphorus showed the highest extraction (89.8%, 9.5 g L^{-1}) among the elements, whereas calcium and iron demonstrated very similar behavior (approximately 30%).

4. Discussion

Goethite is the main iron-bearing mineral for the BEDE sample (Figure 1). During the intense leaching conditions used in the industry to recover REE, iron phases will also solubilize. Gontijo et al. [19] investigated the sulfation reaction kinetics for different high-purity iron oxyhydroxides samples at low-temperatures (80 to 240 °C). At 80 °C, the authors observed that iron fraction varied from 70% to 2% for the different minerals, and goethite represented the sample with the highest reacted fraction. In addition, the authors reported no significant variation of goethite dissolution over temperatures up to 240 °C. Even though the conditions were favorable (i.e., high surface area and porosity, and temperature) to the reaction, the conversion levels in all temperatures remained within 70%–80%.

Figure 3 also shows no significant variation in iron dissolution for sulfation in temperatures from 80 to 240 °C, although iron dissolution is significantly lower (30%) here than those (70%–80%) previously reported by Gontijo et al. [19]. This difference can be assigned to the (i) different goethite contents in the pure and BEDE samples, (ii) higher (3.2x) SSA of the pure sample compared to the BEDE $\text{SSA}_{240 \text{ °C}}$, (iii) differences in the leaching temperature, and (iii) presence of other acid competitors in the BEDE and SILX samples. The reduction in REE extraction with the increase in temperature can be associated with the amount of H_2SO_4 consumed by iron dissolution from goethite between 25 and 160 °C (Figure 3), which is ten times greater the amount of acid required for REE extraction in the same temperature range.

The 0.95:1 H_2SO_4 :sample ratio (Figure 4a) refers to the stoichiometric amount of sulfuric acid contemplating all acid-consuming minerals in BEDE. Even so, the sulfuric acid available for the sulfation reaction was not sufficient to fully decompose the sample. On the contrary, iron dissolution was the lowest compared to all other sub-stoichiometric conditions. The SEM images and EDS analysis for the dissolution residue show very fine iron oxide particulates on the surface of different minerals (e.g., titanium-rich phase, crandallite, calcium-phosphate phase) (Figure 6). Figure 7 shows the element distribution for Ca- and Ce-phosphate-rich phases, which corresponds to monazite encapsulated by a Ca-phosphate phase. Even with the increase in temperature, H_2SO_4 :sample mass ratio and time, the overall REE extraction did not surpass 93%.

The stoichiometric condition in relation to sulfuric acid for BEDE (0.95:1) demonstrates to be selective for the extraction of REE over the dissolution of iron, phosphate, and calcium but the product did not show good handling characteristics. Under strong acidic and high sulfate concentrations, iron can precipitate as iron oxyhydroxides or oxyhydroxysulfate. In that case, the high sulfate concentration hinders mass transfer, creating a local iron saturation zone close to the product dissolution front [30] that favors the formation of iron oxyhydroxides. The precipitation may explain the drop in iron dissolution.

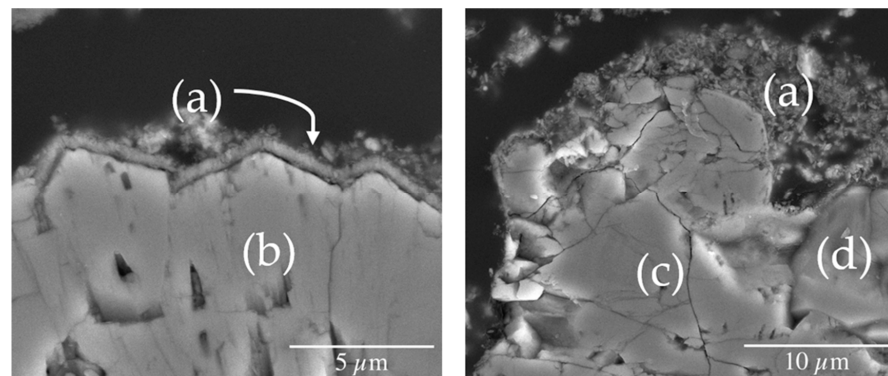


Figure 6. Polished section SEM images of the leaching residue of the sulfation product for BEDE (sulfation at: 25 °C, 30 min 0.95:1 and leaching at 30 ± 3 °C at 0.9 mol L⁻¹ H₂SO₄ for 2 h). (a) Iron oxides, (b) titanium-rich phase, (c) crandallite, and (d) cerium-rich phase.

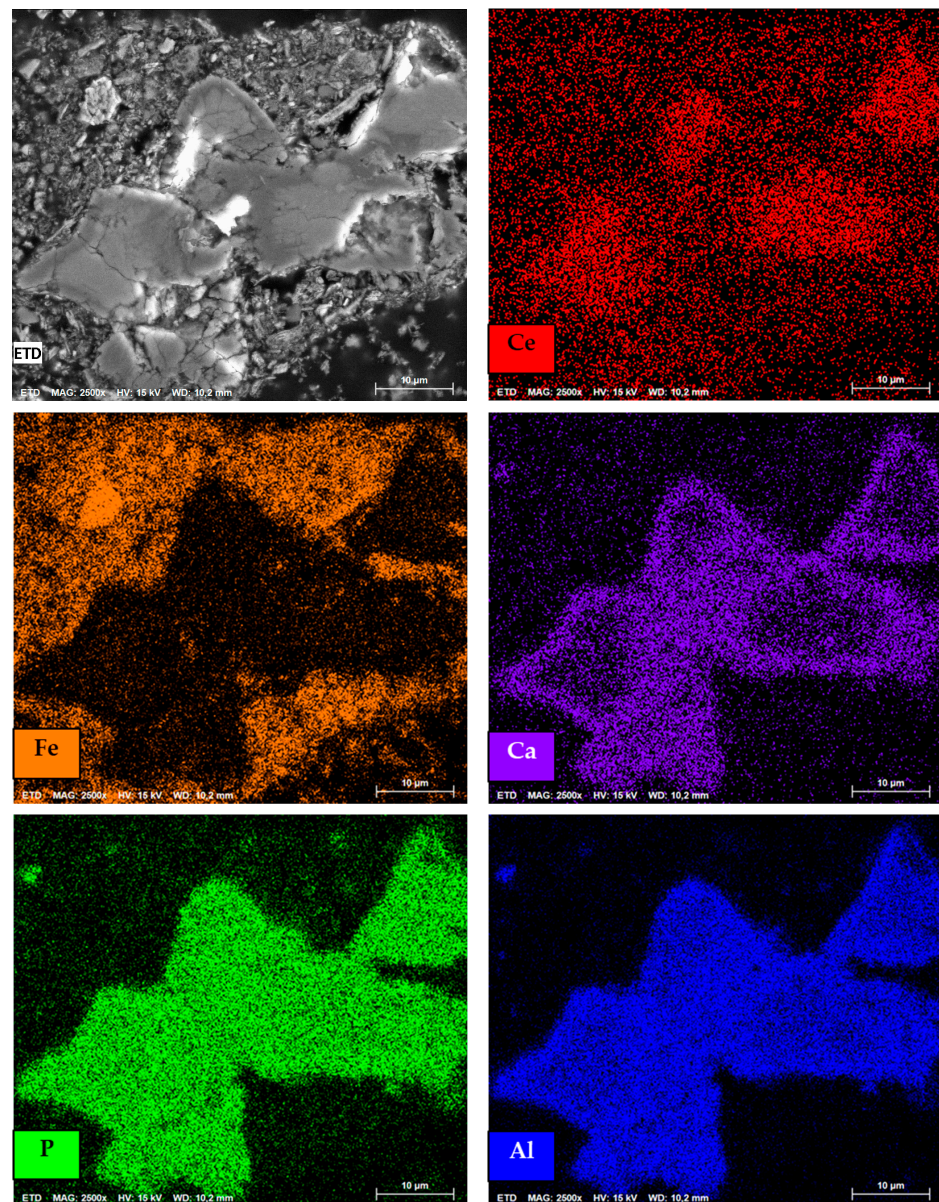


Figure 7. Polished section SEM images for the BEDE leach residue, after sulfation at 25 °C, 30 min and 0.95:1, and leaching at 30 ± 3 °C at 0.9 mol L⁻¹ H₂SO₄ for 2 h.

According to Figure 4 (H_2SO_4 :solid ratios), REE extraction was not affected by the formation of iron oxyhydroxides, which agrees with the results postulated by [31–33]. These studies showed no REE uptake at $\text{pH} < 2$ that during the precipitation of schwertmannite, goethite and ferrihydrite. In sulfate-based acid solutions, the goethite surface charge becomes neutral due to the adsorption of negatively charged sulfate groups. An iron-sulfate speciation diagram (Figure 8) was built with the equilibrium equations of adsorbed species and the adsorption constants for SO_4^{2-} according to [34,35]. The authors observed that SO_4 adsorption reaches 80% at low pH values and is reduced to approximately 0% when pH is increased to 9. The $\equiv\text{Fe}_{(x)}\text{HSO}_4^0$ predominates up to $\text{pH} = 5$ followed by the negatively charged species ($\equiv\text{Fe}_{(x)}\text{HSO}_4^-$) from pH 5 to 7.8. As pH increases, the neutral and negative iron hydroxocomplexes ($\text{pzc}_{\text{goethite}} = 8.9$ —[36]) are formed. It can be inferred that the presence of sulfate hinders cations uptake at $\text{pH} < \sim 4$.

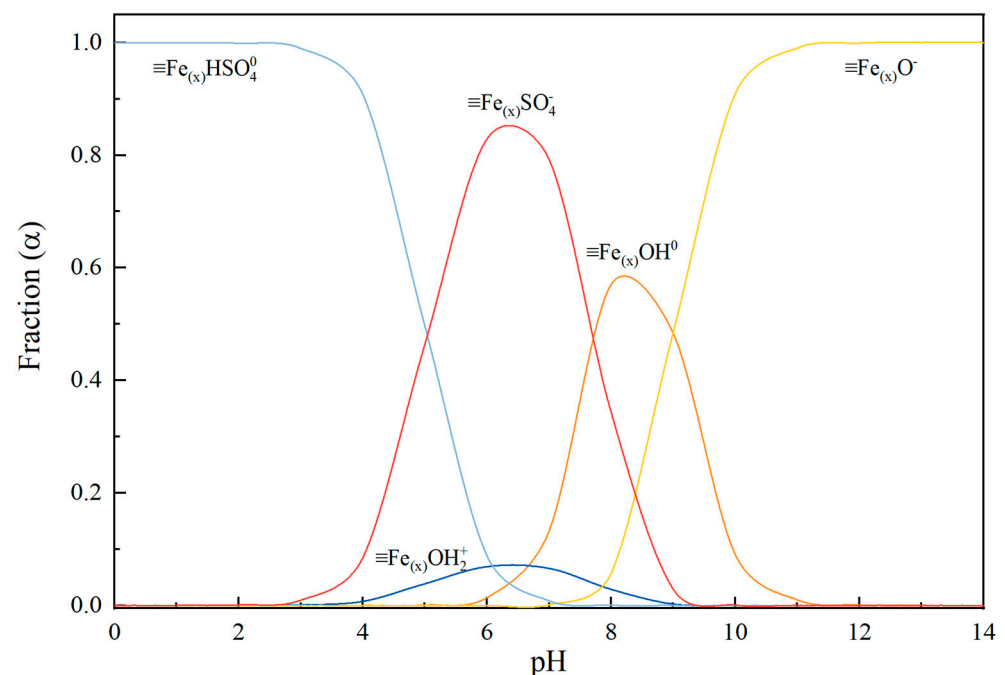


Figure 8. Schematic representation of the distribution of positive, negative, and neutral surface hydroxyl and sulfate groups on the goethite surface with a $\text{pK}_{a1(\text{int})} = 6.7$ and $\text{pK}_{a2(\text{int})} = 9.0$ [35], and $\log K_1^{\text{INT}} (\equiv \text{FeHSO}_4^0) = 12.81$ and $\log K_2^{\text{INT}} (\equiv \text{FeHSO}_4^-) = 7.78$ [34] at 25°C . $\equiv \text{Fe}_{(x)}\text{OH}$ denotes a type-1 or type-2 surface hydroxyl group.

A lower level of impurity dissolution is beneficial to an industrial operation, which favors the sulfation of iron-rich ores, such as BEDE, at room temperature. The lowest and the highest H_2SO_4 :solid ratios exhibited the best REE extraction associated with the minimization of iron, calcium, and phosphorus dissolution.

The REE extraction from SILX (63%) is significantly lower than that from BEDE (92%). Figure 3b shows that temperature does not significantly influence REE extraction nor Ca for temperatures above 80°C , but it favors the increase in iron dissolution up to 45% (6.8 g L^{-1}) and a drop in P. The relatively high P/Fe ratio (Table 1) in SILX and the reduction in phosphorus dissolution at 240°C suggest the formation of insoluble phosphate phases (e.g., monocalcium phosphate), as previously observed in a former work [37] and predicted (i.e., $\text{FePO}_4 \cdot 2\text{H}_2\text{O}$) by thermodynamic simulations [38]. The formation of a monocalcium phosphate compound would increase the viscosity during the sulfation reaction, hindering the overall extraction by incomplete mixture. Indeed, iron and phosphorus can be removed from the leachate when processing iron-rich monazite ores [39]. The XRD analyses showed no evidence of any iron phosphate phases either in the leach residue (not shown) or in the feed material (Figure 1). However, a very fine precipitate formed during the storage of

the leachate was identified as a hydrated ferric phosphate phase by Raman Spectroscopy (Figure S5). Therefore, the reduction in phosphorus dissolution depicted in Figure 3b could be associated with the formation of this insoluble phase.

The precipitation of a REE-bearing phase is not expected according to thermodynamic simulations [38]. Hence, the low extraction for REE may have been associated with other two factors: (i) gypsum formation on the surface of fluorapatite hindering the reaction with H_2SO_4 to proceed, hence, further REE extraction [40], and (ii) REE adsorption on the gypsum product layer formed during sulfation [41]. These factors will be discussed in the following paragraphs.

The formation of a calcium sulfate product layer was observed in the SILX's leaching residue. The SEM chemical mapping of the residue shown in Figure 9 demonstrates an inner calcium-phosphorus core surrounded by a cerium-phosphorus phase, as apatite and monazite. A calcium-sulfur layer (likely gypsum) was detected over the phosphate phases. Hence, the newly formed phase hindered the sulfation reaction and entrapped the remaining REE and P. The REE adsorption on gypsum was evaluated by comparing the XRD of the residues after sulfation (at 25 and 240 °C) and dissolution.

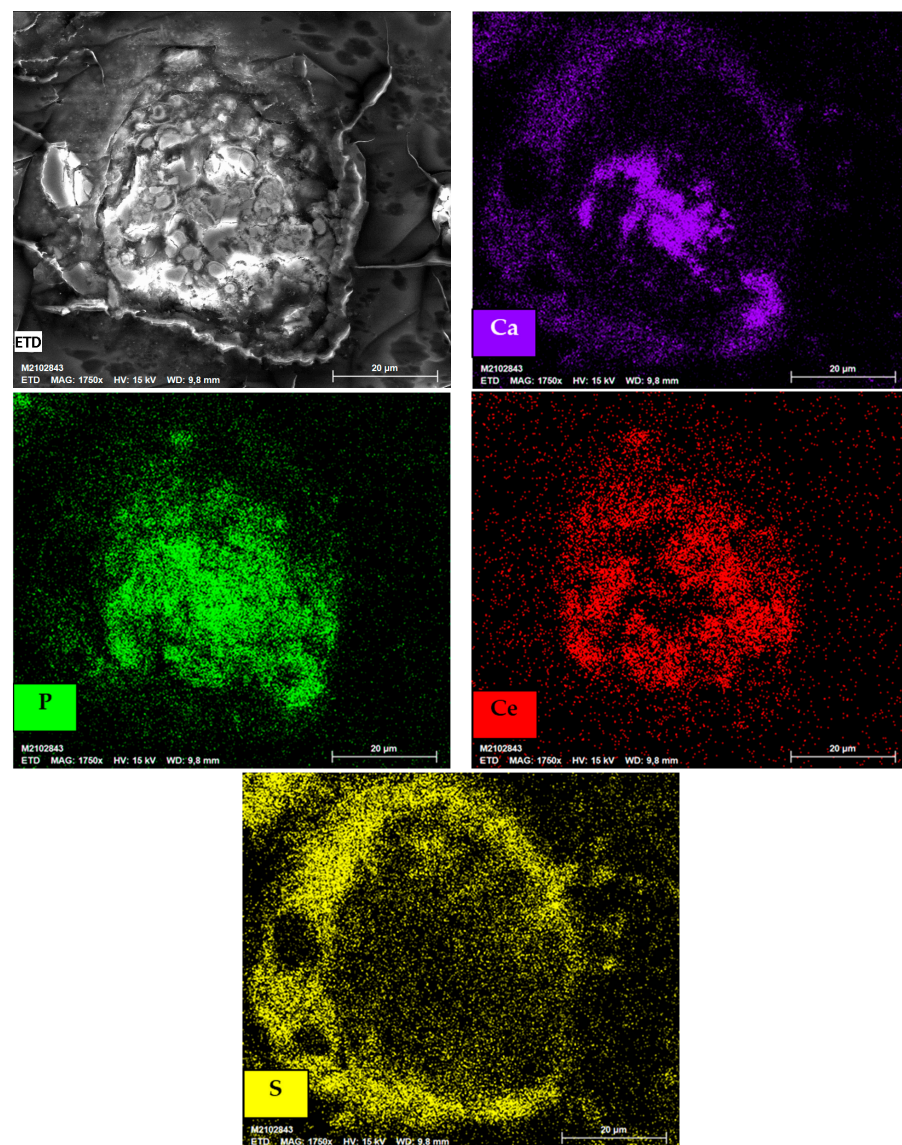


Figure 9. Chemical mapping by EDS showing the calcium sulfate coating on a fluorapatite particle, after sulfation and dissolution of the SILX sample (Sulfation-240 °C; 30 min; sulfuric acid:sample (w/w) 0.45:1).

The diffractograms (Figure 10) indicate two groups based on the drying condition of the leaching residues: (i) 60 °C (Figure 10a,c), and (ii) room temperature (Figure 10b,d), both overnight. Dorozhkin [42] suggested the development of a calcium-rich layer as a “positively charged layer containing strongly adsorbed calcium ions” onto the apatite’s particles. This positive calcium layer in contact with a concentrated sulfate solution favors the formation of a calcium sulfate coating. Battsengel et al. [40] studied the REE recovery from a fluorapatite deposit. The authors also suggested that the non-leached apatite particles were coated by a layer of gypsum. This phenomenon may explain the 63% REE extraction in SILX, a mineral assembly rich in calcium and phosphate.

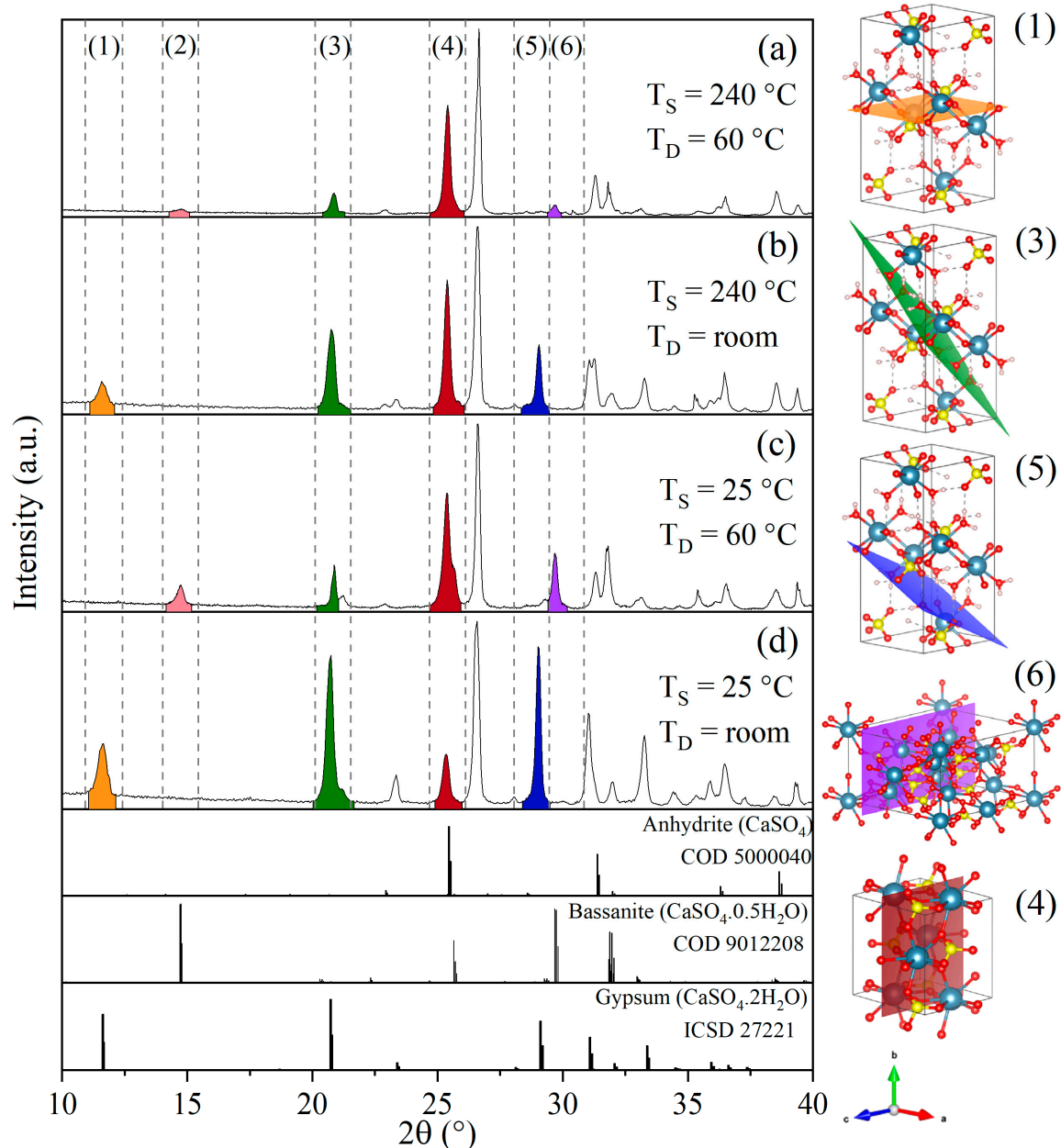


Figure 10. Comparative X-ray diffraction patterns for the SILX leach residues following sulfation at (a,b) 240 °C and (c,d) 25 °C. (a,c) the wet cake dried in an oven at 60 °C, and (b,d) at room temperature, both overnight. Gypsum planes: (1) (020) (orange), (3) (12-1) (green) and (5) (14-1) (blue); Bassanite planes: (2) (1-10) and (6) (400) (purple); and Anhydrite plane: (4) (200) (red). Blue spheres represent calcium, yellow spheres sulfur, red spheres oxygen and pink spheres hydrogen atoms. (T_S = sulfation temperature, T_D = drying temperature).

Dutrizac [41] investigated the deportment of trivalent rare earth elements during gypsum precipitation. The XRD for the precipitated gypsum presented by the authors depicted an interesting behavior. In the presence of REE, the peak intensity of the gypsum (020) plane (Figure 10, orange) ($2\theta = 11.6328^\circ$, $d = 7.6010 \text{ \AA}$) was higher than the typically most intense peak (12-1) (green) ($2\theta = 20.7310^\circ$, $d = 4.2812 \text{ \AA}$) (ISCD 27221). This feature was also observed by [5,40,43] and was ascribed to the inhibitory effect of lanthanides on the rate of gypsum crystallization at the {010} planes. Vreugd et al. [44] observed that gypsum crystals depicted blank macrosteps in the {010} planes in the presence of REE trivalent ions, which corresponds to growth retardation of the planes parallel to the c-axis. Consequently, the b-axis thickness decreases and the crystal grows towards the c- and a-axis. Therefore, the intensity corresponding to the (020) plane increased, whereas the other planes decreased.

In contrast to [40,41,43] the (020) plane peak intensity for gypsum in the present work showed a reduction (Figure 10) relative to the main gypsum peak (green, $2\theta = 20.7310^\circ$). Gypsum was not crystallized in the presence of REE ions, but the insoluble calcium sulfate product layer was formed directly onto the apatite surface. During leaching, the REEs in solution were adsorbed on the (020) plane, and the intensity of the associated peak reduced due to the inhibitory effect. Therefore, the reduction of REE extraction is assigned to the adsorption of REE on gypsum.

For the sulfation at 240°C and residues dried at room temperature (Figure 10b), the gypsum characteristic peaks (i.e., (020), (12-1) and (14-1) ($2\theta = 29.1165^\circ$, $d = 3.0645 \text{ \AA}$) planes) have lower intensities when compared to the 25°C residue (Figure 10d). This feature can be assigned to the dehydration of gypsum, hence reducing the characteristic peaks for this phase. For anhydrite, the peak for the (200) ($2\theta = 25.4613^\circ$, $d = 3.4955 \text{ \AA}$) plane remains consistent for all diffractograms. Moreover, it is apparent that gypsum and anhydrite phases were formed during sulfation/drying.

Heating the leach residue at 60°C played a fundamental role in the partial dehydration of gypsum and the formation of bassanite ($\text{CaSO}_4 \cdot 0.5\text{H}_2\text{O}$). Comparing the diffractograms in relation to the drying condition, it can be observed that after heating the residues at 60°C (Figure 10a,c), there is a reduction of the gypsum peak intensity for both residues. Those changes are more evident when analyzing the 240°C sulfation temperature residue (Figure 10b). Furthermore, the characteristic peaks for gypsum (1) shifted to those corresponding to the bassanite (2). As the temperature increased, fluorine was likely removed by the formation of $\text{HF}_{(g)}$, even though REE and phosphorus were not fully extracted, and Figure 9 shows the presence of encapsulated Ca-P-rich phase. Resin-in-leach technologies can be used in systems containing high calcium content to avoid REE uptake from gypsum. Kurkinen et al. [45], applied this technique in a phosphogypsum waste and good selectivity between calcium and REE was achieved, with 94% REE recovery, and 96% pure. In addition, using intense agitation during sulfation could favor the REE extraction by removing the product layer (i.e., calcium sulfate phases) and exposing fresh REE-bearing minerals to react with H_2SO_4 .

In summary, the experimental conditions of $t = 15 \text{ min}$, H_2SO_4 :sample (w/w) mass ratio of 0.45:1, and sulfuric acid bake at 25°C demonstrated to be more selective for the extraction of REE in relation to the dissolution of impurities for both samples. For BEDE, the sample was more susceptible to react with sulfuric acid, resulting in higher element extractions (12% Fe, 85% TREE). On the other hand, the Ca-rich sample (SILX) had higher phosphate extraction (88%), with REE extraction of 55%. The subsequent purification of the samples described in this work is discussed elsewhere [46–48].

5. Conclusions

The low-temperature ($<300^\circ\text{C}$) acid baking was assessed for two waste rock samples collected in a phosphate mine. The samples differ by the iron and calcium/silica contents, and REE-bearing minerals. The two materials were selected to be used as a case study for the effect of iron- and calcium-rich samples on the recovery of rare earth elements (REE).

For the iron-rich sample, the increase in temperature shows a reduction of REE extraction associated with an increase in iron dissolution. The reduction of REE extraction was assigned to the consumption of sulfuric acid by goethite (a major constituent of the sample). For the effect H₂SO₄:solid ratios, the opposite was observed. Increasing the amount of sulfuric acid (0.95:1 (w/w)) was beneficial to the reduction of iron extraction. This reduction was ascribed to a local iron saturation zone close to the dissolution front, which resulted in the precipitation of iron oxyhydroxides. However, the issues associated with more concentrated acid solutions (i.e., a substantial amount of sulfuric acid, agglomeration), make this approach less attractive.

For the Ca-rich samples, although the REE extraction at 25 °C was the lowest, the increase in temperature reduces the selectivity of the process. Increasing the sulfuric acid amount did not affect the extraction of REE, calcium, and phosphorus. On the other hand, the highest ratio (0.95:1) increased iron extraction by 2x in relation to the lowest ratio (0.45:1). The stabilization of REE extraction was assigned to two factors: (i) entrapment of these elements by the formation of a calcium-sulfate layer on the unreacted fluorapatite, and (ii) by selective adsorption onto the calcium sulfate phases. The latter was ascribed to the inhibitory effect of lanthanides on the formation of the (020) plane on gypsum, which showed a reduction in its intensity compared to the standard gypsum. In addition, increasing the drying temperature for the sulfation residue favored the transformation to bassanite and anhydrite. The high concentration of phosphate and calcium can lead the formation of undesired compounds, that increase the viscosity during sulfation, hindering the extractions by an incomplete reaction.

Supplementary Materials: The following supporting information can be downloaded at: <https://www.mdpi.com/article/10.3390/min13020217/s1>, Figure S1: Chemical mapping by EDS of the polished section for the monazite particle of the as-received BEDE sample; Figure S2: Chemical mapping by EDS of the polished section of crandallite particle of the as-received BEDE sample; Figure S3: Chemical mapping by EDS of the polished section of (a) calcium phosphate (likely fluorapatite) and (b) monazite particle of the as-received SILX sample; Figure S4: Chemical mapping by EDS of the polished section of calcium-cerium phosphate (likely fluorapatite) particle from the as-received SILX sample; Figure S5: Raman spectra of the identified solid precipitated in the final stored solution from the dissolution step of the sulfation product. (a) and (b) hydrated iron phosphate [49]. (Leaching condition: 0.9 mol L⁻¹ H₂SO₄ solution, 30 ± 3 °C for 2 h, final pH = 0.8).

Author Contributions: V.L.G.: data curation, formal analysis, methodology, validation, original draft preparation, investigation; L.A.V.T.: methodology, investigation, reviewing; V.S.T.C.: supervision, conceptualization, formal analysis, funding acquisition, reviewing. All authors have read and agreed to the published version of the manuscript.

Funding: This research received no external funding.

Acknowledgments: The authors would like to thank the funding agencies, CNPq–Conselho Nacional de Desenvolvimento Científico e Tecnológico, CAPES–Coordenação de Aperfeiçoamento de Pessoal de Nível Superior–Brasil–Finance Code 001, and FAPE-MIG–Fundação de Amparo à Pesquisa de Minas Gerais (Renovamin network). A special thanks to Carlos Antônio Morais and Ana Cláudia Queiroz Ladeira for their invaluable contributions to improving this manuscript and for the helpful discussions.

Conflicts of Interest: The authors declare no conflict of interest.

References

1. Gupta, C.K. Krishnamurthy. In *Extractive Metallurgy of Rare Earths*; CRC Press: Boca Radon, FL, USA, 2005.
2. Lucas, J.; Lucas, P.; Le Mercier, T.; Rollat, A.; Davenport, W. Extracting Rare Earth Elements from Concentrates. In *Rare Earth: Science, Technology, Production and Use*; Elsevier Inc: Amsterdam, The Netherlands, 2015; pp. 50–54.
3. Sousa Filho, P.C.; Serra, O.A. Rare Earths in Brazil: History, production and perspectives. *Química Nova* **2014**, *37*, 753–760. (In Portuguese) [[CrossRef](#)]

4. Ribagnac, P.; Deblonde, G.J.P.; Blancher, S.B.; Lengagne, L.; Donati, L.; Malimba, C.; Courtaud, B.; Weigel, V.; Beltrami, D. Leaching of niobium- and REE-bearing iron ores: Significant reduction of H₂SO₄ consumption using SO₂ and activated carbon. *Sep. Purif. Technol.* **2017**, *189*, 1–10. [[CrossRef](#)]
5. Walawalkar, M.; Nichol, C.K.; Azimi, G. Process investigation of the acid leaching of rare earth elements from phosphogypsum using HCl, HNO₃, and H₂SO₄. *Hydrometallurgy* **2016**, *166*, 195–204. [[CrossRef](#)]
6. Beltrami, D.; Deblonde, G.J.P.; Bélair, S.; Weigel, V. Recovery of yttrium and lanthanides from sulfate solutions with high concentration of iron and low rare earth content. *Hydrometallurgy* **2015**, *157*, 356–362. [[CrossRef](#)]
7. Wang, L.; Long, Z.; Huang, X.; Yu, Y.; Cui, D.; Zhang, G. Recovery of rare earths from wet-process phosphoric acid. *Hydrometallurgy* **2010**, *101*, 41–47. [[CrossRef](#)]
8. Vaughan, J.; Tungpalan, K.; Fox, A.P.; Fu, W.; Gagen, E.; Nkruman, P.N.; Southam, G.; Ent, A.V.D.; Erskine, P.D.; Gow, P.; et al. Toward closing a loophole: Recovering rare earth elements from uranium metallurgical process tailings. *JOM* **2020**, *73*, 39–53. [[CrossRef](#)]
9. Hamza, M.F.; El-Aassy, I.E.; Guibal, E. Integrated treatment of tailing material for the selective recovery of uranium, rare earth elements and heavy metals. *Miner. Eng.* **2019**, *133*, 138–148. [[CrossRef](#)]
10. Rychkov, V.N.; Kirillov, E.V.; Kirillov, S.V.; Semenishchev, V.S.; Bunkov, G.M.; Botalov, M.S.; Smyshlyayev, D.V.; Malyshev, A.S. Recovery of rare earth elements from phosphogypsum. *J. Clean. Prod.* **2018**, *196*, 674–681. [[CrossRef](#)]
11. Weshahy, A.R.; Gouda, A.A.; Atia, B.M.; Sakr, A.K.; Al-Otaibi, J.S.; Almuqrin, A.; Hanfi, M.Y.; Sayyed, M.I.; El Sheikh, R.; Radwan, H.A.; et al. Efficient recovery of rare earth elements and zinc from spent Ni-metal hydride batteries: Statistical studies. *Nanomaterials* **2022**, *12*, 2305. [[CrossRef](#)]
12. Önal, M.A.R.; Borra, C.R.; Guo, M.; Blanpain, B.; Gerven, T.V. Hydrometallurgical recycling of NdFeB magnets: Complete leaching, iron removal and electrolysis. *J. Rare Earths* **2017**, *35*, 574–584. [[CrossRef](#)]
13. Lee, C.H.; Chen, Y.J.; Liao, C.H.; Popuri, S.R.; Tsai, S.L.; Hung, C.E. Selective leaching process for neodymium recovery from scrap Nd-Fe-B magnet. *Metall. Mater. Trans. A* **2013**, *44*, 5825–5833. [[CrossRef](#)]
14. Agência Nacional De Mineração (ANM). *Sumário Mineral*; Ministério de Minas e Energia: Brasil, Brazil, 2017; pp. 164–166.
15. Louwse, D. Rare Earth Element Deposits and Occurrences within Brazil and India. Bachelor's Thesis, Delft University of Technology, Delft, The Netherlands, 2016.
16. Vieira, E.V.; Lins, F.F. Processos Industriais de Concentração. In *Concentração de Minérios de Terras-Raras: Uma Revisão*; CETEM/CNPq: Rio de Janeiro, Brazil, 1997; Volume 7, pp. 19–32. (In Portuguese)
17. Koopman, C.; Witkamp, G.J. Extraction of lanthanides from the phosphoric acid production process to gain a purified gypsum and a valuable lanthanide by-product. *Hydrometallurgy* **2000**, *58*, 51–60. [[CrossRef](#)]
18. Habashi, F. Extractive metallurgy of rare earths. *Can. Metall. Q.* **2013**, *52*, 224–233. [[CrossRef](#)]
19. Gontijo, V.L.; Teixeira, L.A.V.; Ciminelli, V.S.T. The reactivity of iron oxides and hydroxide during low-temperature sulfation. *Hydrometallurgy* **2020**, *197*, 105452. [[CrossRef](#)]
20. Ribeiro, P.P.M.; Neumann, R.; Santos, I.D.; Rezende, M.C.; Rouse, P.R.; Dutra, A.J.B. Nickel carriers in laterite ores and their influence on the mechanism of nickel extraction by sulfation-roasting-leaching process. *Miner. Eng.* **2019**, *131*, 90–97. [[CrossRef](#)]
21. Teixeira, L.A.V.; Silva, R.G.; Avelar, A.; Majuste, D.; Ciminelli, V.S.T. Selective Extraction of Rare Earth Elements from Monazite Ores with High Iron Content. *Min. Metall. Explor.* **2019**, *36*, 235–244. [[CrossRef](#)]
22. Kar, B.B.; Swamy, Y.V. Some aspects of nickel extraction from chromitiferous overburden by sulphatization roasting. *Miner. Eng.* **2000**, *13*, 1635–1640. [[CrossRef](#)]
23. Bainbridge, D.W. Sulfation of a Nickeliferous Laterite. *Metall. Trans.* **1973**, *4*, 1655–1658. [[CrossRef](#)]
24. Zhang, J.; Zhao, B.; Schreiner, B. *Separation Hydrometallurgy of Rare Earth Elements*; Springer: Berlin/Heidelberg, Germany, 2016.
25. Soubiés, F.; Melfi, A.J.; Autefage, F. Geochemical behavior of rare earth elements in alterites from the Tapira phosphate and titanium deposit (Minas Gerais, Brazil): The importance of phosphates. *Rev. Bras. Geociências* **1991**, *21*, 3–16. (In Portuguese)
26. Delvigne, J.E. *Atlas of Micromorphology of Mineral Alteration and Weathering*; Mineralogical Association of Canada: Ottawa, ON, Canada, 1998.
27. Santos, R.L.C.; Sobral, L.G.S.; Araújo, R.V.V. Phosphate Production in Brazil: Tapira/Fosfertil Mining Complex. In Proceedings of the Encontro Nacional de Tratamento de Minérios e Metalurgia Extrativa, Recife, Brazil, 26–29 November 2002; Volume 1, pp. 439–445. (In Portuguese).
28. Verbaan, N.; Bradley, K.; Brown, J.; Mackie, S. A review of hydrometallurgical flowsheets considered in current REE projects. In *Symposium on Strategic and Critical Materials Proceedings*; Simandl, G.J., Neetz, M., Eds.; British Columbia Ministry of Energy and Mines: Victoria, BC, Canada, 2015; Volume 3, pp. 147–162.
29. Demol, J.; Ho, E.; Soldenhoff, K.; Senanayake, G. The Sulfuric Acid Bake and Leach Route for Processing of Rare Earth Ores and Concentrates: A Review. *Hydrometallurgy* **2019**, *188*, 123–139. [[CrossRef](#)]
30. Thibault, Y.; McEvoy, J.G. Minimizing the impact of passivation during allanite-(Ce) decomposition in sulfuric acid media for rare earth recovery. *Miner. Pet.* **2020**, *144*, 559–571. [[CrossRef](#)]
31. Lozano, A.; Ayora, C.; Martínez, A.F. Sorption of rare earth elements on schwertmannite and their mobility in acid mine drainage treatments. *Appl. Geochem.* **2020**, *113*, 104499. [[CrossRef](#)]
32. Dutrizac, J.E.; Soriano, C. Behaviour of the rare earths during goethite (α -FeOOH) precipitation from sulphate-based solutions. *Hydrometallurgy* **2018**, *176*, 87–96. [[CrossRef](#)]

33. Riley, E.; Dutrizac, J.E. The behavior of the rare earth elements during the precipitation of ferrihydrite from sulphate media. *Hydrometallurgy* **2017**, *172*, 69–78. [[CrossRef](#)]
34. Swedlund, P.J.; Webster, J.G.; Miskelly, G.M. Goethite adsorption of Cu(II), Pb(II), Cd(II), and Zn(II) in the presence of sulfate: Properties of the ternary complex. *Geochim. Cosmochim. Acta* **2009**, *73*, 1548–1562. [[CrossRef](#)]
35. Müller, B.; Sigg, L. Adsorption of Lead(II) on the goethite surface: Voltammetric Evaluation of surface complexation parameters. *J. Colloid Interface Sci.* **1992**, *148*, 517–532. [[CrossRef](#)]
36. Cornell, R.M.; Schwertmann, U. *The Iron Oxides: Structure, properties, Reactions, Occurrence and Uses*, 2nd ed.; VCH: Weinheim, Germany, 2003.
37. Teixeira, L.A.V.; Silva, R.G.; Majuste, D.; Ciminelli, V.S.T. Stability of lanthanum in sulfate and phosphate systems and implications for selective rare earths extraction. *Miner. Eng.* **2020**, *155*, 106440. [[CrossRef](#)]
38. Gontijo, V.L.; Teixeira, L.A.V.; Majuste, D.; Ciminelli, V.S.T. A review of thermodynamic data for lanthanum, iron, and thorium applied to rare earth extraction. *Hydrometallurgy* **2022**, *213*, 105951. [[CrossRef](#)]
39. Li, H.; Zhao, N.; Zhang, G.; Liu, Y.; Long, Z.; Huang, X.; Griem Advanced Materials Co., Ltd. A Process of Smelting Monazite Rare Earth Ore Rich in Fe. Patent AU 2008286599, 18 November 2010.
40. Battsengel, A.; Batnasan, A.; Narankhuu, A.; Haga, K.; Watanabe, Y.; Shibayama, A. Recovery of light and heavy rare earth elements from apatite ore using sulfuric acid leaching, solvent extraction and precipitation. *Hydrometallurgy* **2018**, *179*, 100–109. [[CrossRef](#)]
41. Dutrizac, J.E. The behavior of the rare earth elements during gypsum (CaSO₄·2H₂O) precipitation. *Hydrometallurgy* **2017**, *174*, 38–46. [[CrossRef](#)]
42. Dorozhkin, S.V. Dissolution mechanism of calcium apatites in acids: A review of literature. *World J. Methodol.* **2012**, *2*, 1–17. [[CrossRef](#)] [[PubMed](#)]
43. Sadri, F.; Kim, R.; Yang, Z.; Ghahreman, A. The effect of calcium sulfate crystallization and the crystal modification on aqueous REE stability in Ca saturated REE-Ca-SO₄-H₂O systems. *Hydrometallurgy* **2018**, *182*, 82–96. [[CrossRef](#)]
44. Vreugd, C.H.; Witkamp, G.J.; Rosmalen, G.M. Growth of gypsum III. Influence and incorporation of lanthanide and chromium ions. *J. Cryst. Growth* **1994**, *144*, 70–78. [[CrossRef](#)]
45. Kurkinen, S.; Virolainen, S.; Sainio, T. Recovery of rare earth elements from phosphogypsum waste in resin-in-leach process by eluting with biodegradable complexing agents. *Hydrometallurgy* **2021**, *201*, 105569. [[CrossRef](#)]
46. Silva, R.G.; Morais, C.A.; Oliveira, E.D. Evaluation of different neutralization reagents in the selective removal of impurities in rare earth sulfuric liquor. *Min. Metall. Explor.* **2020**, *37*, 65–78. [[CrossRef](#)]
47. Silva, R.G.; Morais, C.A.; Oliveira, E.D. Selective precipitation of rare earth from non-purified sulfate liquors using sodium sulfate and disodium hydrogen phosphate. *Miner. Eng.* **2019**, *134*, 402–416. [[CrossRef](#)]
48. Silva, R.G.; Morais, C.A.; Teixeira, L.V.; Oliveira, E.D. Selective precipitation of high-quality rare earth oxalate or carbonates from a purified sulfuric liquor containing soluble impurities. *Min. Metall. Explor.* **2019**, *36*, 967–977. [[CrossRef](#)]
49. Larroumet, D.; Greenfield, D.; Akid, R.; Yarwood, J. Spectroscopic studies of the corrosion of model iron electrodes in carbonate and phosphate buffer solutions. *J. Raman Spectrosc.* **2008**, *39*, 1740–1748. [[CrossRef](#)]

Disclaimer/Publisher’s Note: The statements, opinions and data contained in all publications are solely those of the individual author(s) and contributor(s) and not of MDPI and/or the editor(s). MDPI and/or the editor(s) disclaim responsibility for any injury to people or property resulting from any ideas, methods, instructions or products referred to in the content.